

Stability analysis on the effect of a smooth surface hump on secondary instabilities of crossflow vortices

Biagio Ambrosino ^{§*†}, Mohammad Moniripiri ^{¶†}, Marios Kotsonis [‡], Ardeshir Hanifi [¶] and Stefan Hein ^{*}

^{*} German Aerospace Center, Department of High-Speed Configurations,
Institute of Aerodynamics and Flow Technology, 37073 Göttingen, Germany

[§] Universidad Politécnica de Madrid, Plaza Cardenal Cisneros 3, E-28040 Madrid, Spain

[¶] FLOW, Department of Engineering Mechanics, KTH Royal Institute of Technology,
10044 Stockholm, Sweden

[‡] Delft University of Technology, Faculty of Aerospace Engineering, Department of Flow Physics and Technology,
TU Delft, Kluyverweg 1, 2629 HS, Delft, The Netherlands

biagio.ambrosino@dlr.de · momp@kth.se

[†] Corresponding author

Abstract

This work demonstrates that linear stability analysis can be used to study the effect of a smooth hump on secondary instabilities in incompressible swept-wing boundary layers. Two-dimensional Local Stability Theory (LST-2D) and three-dimensional Parabolized Stability Equations (PSE-3D) are employed to investigate how secondary crossflow instabilities are affected by the presence of a hump, compared to the reference (without hump) case. Comparisons between PSE-3D and DNS results, for the dominant instability induced by the hump, show good agreement. These findings confirm the capability of PSE-3D as an efficient tool for analyzing secondary instabilities in boundary layers affected by smooth surface humps.

1. Introduction

In recent years, increasing fossil fuel costs and growing environmental concerns have reignited interest in laminar flow control (LFC) technology. The main goal is to reduce skin-friction drag, which accounts for nearly half of the total drag on commercial airliners.¹ To this end, significant research efforts have focused on understanding the laminar-to-turbulent transition process in boundary layers over swept wings. However, maintaining extended laminar flow in real flight conditions remains challenging. This difficulty is largely due to surface irregularities such as steps,^{2,3} roughness,⁴ and waviness,⁵ which strongly influence the laminar-to-turbulent transition over the wings and tails of commercial aircraft.

The boundary layer over swept wings differs from two-dimensional cases due to a favourable leading-edge pressure gradient and a sweep-induced crossflow (CF) component, which vanishes at the wall and the boundary layer's outer inviscid edge. The CF velocity component is inherently inflectional and promotes inviscid CF instabilities.⁶ These instabilities manifest as corotating vortices aligned with the external streamlines of the flow. They are classified as stationary or travelling modes.⁷ Stationary modes, often triggered by surface roughness, dominate in low-turbulence conditions,⁸ while travelling modes become dominant at higher turbulence levels.⁹ Under typical free-flight conditions, stationary crossflow vortices dominate the boundary layer development,⁶ redistributing momentum and breaking spanwise uniformity. This lifts low-momentum fluid upward and drives high-momentum fluid downward, creating strong shear layers prone to rapidly amplifying secondary instabilities.¹⁰⁻¹² These instabilities, which can trigger laminar breakdown, are classified into three types based on their location around the vortex. Type I mode appears on the upwash side where the negative spanwise velocity gradient peaks. Type II instabilities form near the top of stationary crossflow vortices and are driven by wall-normal velocity gradients, differing from type I in structure and amplification. Type III instabilities are low-frequency modes that arise near the wall and result from the interaction between primary travelling and stationary crossflow instabilities.^{10,13-15} In swept-wing boundary layers, crossflow vortices grow near the leading edge and often interact strongly with surface features, such as steps.¹⁶ Eppink¹⁷ found that the impact of a Forward-Facing Step (FFS) depends on the initial vortex amplitude. Rius-Vidales & Kotsonis¹⁸ showed that a small FFS can delay the transition, contradicting earlier findings.^{17,19} Groot & Eppink²⁰ applied two-dimensional Local Stability Theory (LST-2D) to experimental data and identified rapidly growing instabilities, but SPOD analysis revealed discrepancies, highlighting the complexity of step-vortex interactions. Tocci *et al.*²¹ used DNS to investigate

INFLUENCE OF SURFACE HUMP ON SECONDARY CROSSFLOW INSTABILITIES

the influence of FFS in three-dimensional boundary layers, motivated by the experimental findings of Rius-Vidales & Kotsonis,²² who observed a non-monotonic relationship between step height and transition location.

Recently, Rius-Vidales *et al.*²³ investigated the interaction between a smooth surface hump and stationary crossflow vortices of different amplitudes. In their experiments, the primary crossflow instability was induced using discrete roughness elements (DREs) near the leading edge, with the vortex amplitude controlled by the DRE placement. For *high*-amplitude forcing (DREs at 2% of the chord) and in the presence of the hump, transition was observed slightly downstream of the hump at approximately 24% of the chord. Under the same CF forcing conditions, transition occurred at approximately 44% of the chord in a clean (without surface hump) configuration. In contrast, for *low*-amplitude forcing condition (DREs at 5% of the chord), the hump delayed the transition by approximately 14% chord length relative to the clean (without the hump) configuration. For similar flow conditions to the experiments of Rius-Vidales *et al.*,²³ Moniripiri *et al.*²⁴ performed DNS to understand the mechanisms leading to transition delay and transition advancement in both forcing conditions of the experiments. For the *low*-amplitude perturbation case leading to transition delay, they showed that CF velocity reversal occurs downstream of the hump, altering the orientation of stationary CF perturbations. This reduces the lift-up effect and weakens the spanwise gradients, ultimately contributing to transition delay by shifting the neutral point of the type I secondary instability farther downstream compared to the clean case. In the *high*-amplitude perturbation case, DNS revealed the emergence of counter-rotating vortices downstream of the hump, which increased the spanwise gradients in the flow field. This, in turn, promoted the rapid amplification of unsteady secondary instabilities at a frequency of approximately 1100 Hz, ultimately leading to transition downstream of the hump. These findings are in agreement with experimental observations reported in.²³

While DNS provides highly detailed and accurate results, it is computationally expensive for studying the evolution of the secondary crossflow instabilities. The present work employs two-dimensional Local Stability Theory (LST-2D) and three-dimensional Parabolized Stability Equations (PSE-3D), within a linear framework, to investigate secondary crossflow instabilities in three-dimensional base flows previously studied, using DNS, by Moniripiri *et al.*²⁴ LST-2D and PSE-3D provide a computationally efficient alternative to DNS and are well-suited for systematic parametric analyses. The main goal of this work is to illustrate that PSE-3D and LST-2D can be effectively used to analyse secondary crossflow instabilities in three-dimensional boundary layers in the presence of smooth surface hump.

The structure of the paper is as follows. § 2 presents the coordinate systems, geometry, flow configuration, details of the numerical simulations, and the formulation employed for the LST-2D/PSE-3D approaches. Details of the base flows used for the instability computations are given in § 3. § 4 presents the results of the stability analysis downstream of the hump geometries. A quantitative comparison between the instability methodologies and DNS data is provided in § 5. Finally, § 6 provides the concluding remarks of this work.

2. Numerical methodology and flow configuration

This section briefly introduces the different coordinate systems used in this work, the flow configuration under investigation, and the numerical methodology employed for the base flow computation. Moreover, § 2.4 provides the details on the instability methodologies adopted in this work.

2.1 Coordinate systems

This study employs multiple coordinate systems for computation and visualization purposes. DNS (cf. § 2.3) is performed in a Cartesian coordinate system (x_g, y_g, z) , where z is the spanwise direction (parallel to the leading edge), x_g is perpendicular to the leading edge and y_g is normal to those two directions (cf. figure 1). The corresponding velocity components are (u_g, v_g, w_g) . Some results are presented in the curvilinear coordinate system, denoted as (x, η, z) . It has the same origin and the same spanwise coordinate z as the Cartesian coordinate system, with x being tangent to the wing surface and η normal to it. The corresponding velocity components in this frame are denoted as (u_c, v_c, w_c) . Stability results are computed in a non-orthogonal system (ξ, η, ζ) , where ξ aligns with the direction of least variation of the base flow derivatives at each x position and will be referred to as streamwise direction. The ζ -direction is parallel to the leading edge but shifted relative to z , such that $\zeta = 0$ along ξ , while $z = 0$ along x . The contravariant velocity components used in the linearized equations are (u, v, w) , related to the curvilinear ones by:

$$\begin{cases} u = u_c \sec(\theta), \\ w = w_c - u_c \tan(\theta). \end{cases} \quad (1)$$

The angle θ represents the deviation of the ξ -coordinate from the chordwise direction x (see figure 1). The details about the evaluation of the angle θ and its impact on the instability computations can be found in Ambrosino *et al.*²⁵

INFLUENCE OF SURFACE HUMPS ON SECONDARY CROSSFLOW INSTABILITIES

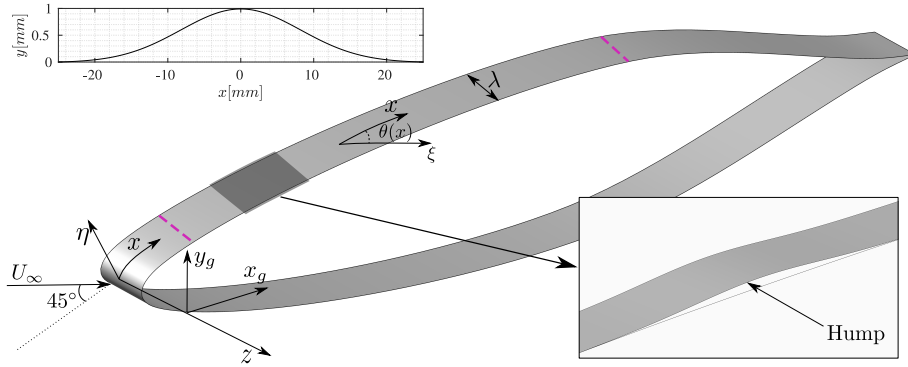


Figure 1: Overview of the geometry alongside the Cartesian (x_g, y_g, z) and the orthogonal curvilinear (x, η, z) coordinate systems. The origin of the Cartesian coordinate system is shifted for an improved visualization in the plot. The insets displays an enlargement around the hump location (bottom) and the smooth hump geometry before projection on the airfoil (top). The two dashed purple lines on the wing mark the location of the inlet ($x/c_x = 0.055$) and outlet ($x/c_x = 0.69$) of the 3D DNS domain, on the pressure side of the wing.

2.2 Flow configuration and hump geometry

The geometry under study is a 45-degree swept wing at an angle of attack of $AoA = -3^\circ$, which mimics the experimental setup of Rius-Vidales *et al.*²³ in the Low Turbulence Tunnel (LTT) at Delft University of Technology. The symmetric airfoil used in the swept-wing model is a modified version of the NACA 66018 geometry¹² (cf. figure 1). Measurements were performed on the pressure side of the wing. The swept wing has a normal to the leading edge chord length $c_x = 0.9$ m. The free stream turbulence intensity is less than 0.03% in the experiment, ensuring that stationary crossflow vortices dominate the laminar-turbulent transition.⁸ The primary crossflow instability is promoted in the experiment with the use of spanwise distributed DREs, with a nominal height of $25 \mu\text{m}$ and placed with a spanwise spacing of $\lambda = 7.5$ mm, corresponding to the wavelength of a critical and dangerous CFI mode reaching high levels of amplification prior to natural transition. Two forcing configurations were tested, with the DREs placed at $x/c_x = 0.02$ (i.e., at 2% of the chord from the leading edge) for the *high*-amplitude perturbation case (referred to as A_2 case) and at $x/c_x = 0.05$ for the *low*-amplitude perturbation case (referred to as A_1 case). In the former setup, the DREs are located closer to the neutral point of the CFI mode, resulting in stronger vortex development at the hump location. The clean geometry, i.e., with no surface hump, is referred to as the reference case. The reference parameters employed in the DNS are listed in table 1. The Reynolds number, based on c_x , is $Re_{c_x} = (\rho_\infty U_\infty c_x) / \mu_\infty \approx 1.68 \times 10^6$.

Table 1: Flow and geometry parameters

Parameter	Symbol	Value
Normal to the leading edge chord length	c_x	0.9 m
Angle of attack	AoA	-3.0°
Free stream velocity	U_∞	26.21 m s^{-1}
Reference pressure	p_∞	$1.03526 \times 10^5 \text{ Pa}$
Reference density	ρ_∞	1.2648 kg m^{-3}
Reference viscosity	μ_∞	$1.77 \times 10^{-5} \text{ kg m}^{-1} \text{ s}^{-1}$
Reynolds number	Re_{c_x}	1.68×10^6 [-]

The hump geometry used in this study is similar to the shape employed in the experimental investigations by Rius-Vidales *et al.*²³ The hump is installed on the pressure side of the airfoil such that its apex is located at a chordwise position of $x/c_x = 0.15$, and it expands over $0.122 \lesssim x/c_x \lesssim 0.177$. The hump is spanwise homogeneous (along the z direction) and features a symmetric concave-convex-concave shape. Its dimensional height is 1 mm, and has a height-to-width ratio of 1:50. The nominal shape of the hump, prior to its projection onto the curved airfoil surface, is illustrated in the upper inset of the figure 1. The resulting wing geometry in the vicinity of the hump, after projection, is depicted in the lower inset of figure 1. The details about the projection of the hump onto the airfoil surface can be found in Moniripiri *et al.*²⁴

2.3 Direct Numerical Simulation

This section briefly describes the setup employed for the DNS. The numerical simulations conducted in Moniripiri *et al.*²⁴ not only provide the steady base flow for the instability analysis, but also provide the unsteady results that are used as a comparison for the secondary instability results from the instability methodology, as will be shown in § 5.

The DNS are carried out using the spectral element method (SEM) code Nek5000.²⁶ Due to the significant computational cost associated with three-dimensional (3D) DNS, these simulations are conducted on the pressure side of the wing, and within a relatively small domain (i.e., $0.055 < x/c_x < 0.69$, cf. figure 1), requiring carefully defined boundary conditions. A two-step approach is implemented to establish these conditions. First, a 2.5D Reynolds-Averaged Navier-Stokes (RANS) simulation is performed on a section of the wind tunnel that includes both the airfoil geometry and tunnel walls. The resulting flow field from this computation provides the far-field boundary conditions for a subsequent 2.5D DNS, which generates a highly accurate spanwise-invariant steady-state flow in an intermediate domain. The output from this second step is then used to define the boundary conditions for the final 3D DNS.

To minimize the computational expenses, the 3D DNS performed here does not account for the generation of crossflow vortices by the DRE arrays, as observed in the experiments. Instead, the stationary crossflow vortices are introduced in the DNS by imposing the crossflow instability (CFI) mode as an inlet boundary condition, superimposed onto the spanwise-invariant base flow obtained from the 2.5D DNS. The shape and amplitude of the CFI mode were matched to the experimental results using nonlinear PSE.²⁷ To accurately replicate the experimental setup of Rius-Vidales *et al.*²³ numerically, the computational domain in the spanwise direction is restricted to a single wavelength, $\lambda = 7.5$ mm, with periodic boundary conditions applied along the spanwise axis. This approach effectively simulates the influence of DREs.

To study transition to turbulence in DNS, as described in § 5, unsteady perturbations are artificially introduced into the boundary layer just downstream of the inflow boundary. This is achieved by applying a randomly pulsed volume force, a technique similar to the 'trip forcing' method described by Hosseini *et al.*²⁸ and employed in Tocci *et al.*²¹ The forcing mechanism is implemented within the momentum equation as a wall-normal force component, selectively introducing perturbations across a defined spectrum of spanwise wavenumbers ($\beta = m\beta_0$, $m = 1, 2, \dots, 16$, $\beta_0 = 2\pi/\lambda$) and frequencies ranging from 1.1 to 10 kHz. The amplitude of the forcing is adjusted to closely recover the experimentally observed transition location for the reference A_1 case, and the same amplitude is used for all simulations. During the post-processing, the velocity field undergoes a Fourier transformation in time, allowing the extraction of individual modes for direct comparison with instability analysis results. More details about the setup of the DNS are provided in Moniripiri *et al.*²⁴

2.4 Instability analysis

To study the evolution of the secondary and hump-induced instabilities, the LST-2D and PSE-3D methodologies formulated in a non-orthogonal coordinate system are employed.²⁵ These are linear theories, which rely on the decomposition of the primitive flow quantities $\mathbf{q} = [p, u, v, w]^T$ into a steady state $\bar{\mathbf{q}} = [\bar{p}, \bar{u}, \bar{v}, \bar{w}]^T$, also referred to as base flow, and a small unsteady perturbation $\tilde{\mathbf{q}} = [\tilde{p}, \tilde{u}, \tilde{v}, \tilde{w}]^T$:

$$\mathbf{q}(\xi, \eta, \zeta, t) = \bar{\mathbf{q}}(\xi, \eta, \zeta) + \epsilon \tilde{\mathbf{q}}(\xi, \eta, \zeta, t), \quad (2)$$

where $\epsilon \ll 1$. Introducing the flow decomposition (2) into the Navier-Stokes equation, and subtracting the terms for the steady flow, which is assumed to satisfy the full Navier-Stokes equations, one obtains the linearized Navier-Stokes equations (LNSE) once the product of the perturbation quantities is neglected.

2.4.1 Two-dimensional Local Stability Theory

The LST-2D theory is based on the assumption of parallel flow, which implies that two spatially inhomogeneous directions have to be solved within a plane, while maintaining spatial homogeneity in the streamwise direction. This assumption is expressed as $\bar{\mathbf{q}} = \bar{\mathbf{q}}(\eta, \zeta)$. The corresponding formulation for modal perturbations is given by:

$$\tilde{\mathbf{q}}(\xi, \eta, \zeta, t) = \hat{\mathbf{q}}(\eta, \zeta) \exp[i(\alpha\xi - \omega t)] + c.c., \quad (3)$$

where $\hat{\mathbf{q}} = [\hat{u}, \hat{v}, \hat{w}, \hat{p}]^T$ is the vector which contains the two-dimensional complex amplitude functions in the plane $\eta\zeta$, α is the wavenumber in the streamwise direction, ω is the circular frequency and *c.c.* represents the complex conjugate. A spatial framework is here employed, which means that ω is the real-valued angular frequency of the eigenfunction, whereas α is complex. The real part of α , α_r , represents the wavenumber of $\hat{\mathbf{q}}$ along the streamwise direction ξ with wavelength $\lambda_\xi = 2\pi/\alpha_r$. The imaginary part, α_i , is related to the growth rate by $\sigma = -\alpha_i$. Note that $\alpha_i < 0$ indicates a perturbation that grows exponentially in the streamwise direction.

2.4.2 Three-dimensional Parabolized Stability Equations

To study the weakly non-parallel effects in convectively unstable flows, such as for the instabilities studied in this work, the parallel flow assumption of the LST-2D can be relaxed, allowing a slow streamwise variation of the base flow and of the perturbation quantities. The disturbance ansatz has the following shape:

$$\tilde{\mathbf{q}}(\xi, \eta, \zeta, t) = \hat{\mathbf{q}}(\xi, \eta, \zeta) \exp \left[i \left(\int_{\xi} \alpha(\xi) d\xi - \omega t \right) \right] + c.c.. \quad (4)$$

Substituting the three-dimensional Parabolized Stability Equations (PSE-3D) ansatz into the LNSE and introducing a scale separation between the weak variation in the streamwise direction and the strong variation in the wall-normal direction, and neglecting terms of order ($O(1/Re^2)$), leads to the non-local linear stability PSE-3D.²⁵ In this case, the growth rate is not only the imaginary part of α , but is given by two contributions. The first term accounts for the exponential part of the perturbation, whereas the second term takes into account the growth associated with the streamwise variation of the amplitude function. It reads as

$$\sigma = -\alpha_i + \frac{\partial}{\partial \xi} \ln(\sqrt{E}), \quad (5)$$

where E is the total kinetic energy, defined as

$$E = \int_{\eta} \int_{\zeta} (|\hat{u}|^2 + |\hat{v}|^2 + |\hat{w}|^2) d\zeta d\eta. \quad (6)$$

In § 4, the instability results are presented in terms of the integrated growth rate (N -factor), which is defined as $N = \int_{\xi_0}^{\xi} \sigma d\xi'$, where σ represents the growth rate in the non-orthogonal coordinate system, ξ_0 indicates the position where a disturbance starts to grow at a certain frequency, and ξ' represents a dummy integration variable for the out-of-plane ξ -direction. The PSE-3D equations form an initial boundary value problem that can be solved by a streamwise marching procedure. The computation is initialised using the eigenvalue solution obtained from LST-2D. In both LST-2D and PSE-3D methodologies, the no-slip condition is imposed at the wall, homogeneous Dirichlet boundary conditions are applied at the upper boundary, while periodic boundary conditions are imposed on the lateral boundaries. The wall-normal and spanwise directions are discretized using the high-order finite-difference scheme FD- q proposed by Hermanns *et al.*,²⁹ with $q = 8$ (eight-order) applied in both directions. In the PSE-3D computations, the streamwise derivative is discretized using an implicit first-order backward Euler scheme.

3. Three-dimensional base flows

This section provides a brief overview of the base flows used in the stability analysis and highlights the influence of the hump on the base flows. The hump affects the pressure distribution over the wing only in its immediate vicinity, as shown in figures 2(a, b). The flow initially accelerates over the hump ($\partial C_p / \partial x < 0$), followed by a short region of adverse pressure gradient (APG) downstream of the apex of the hump, before recovering the nominal favourable pressure gradient (FPG) of the wing. Note that the flow, in the streamwise direction, remains fully attached to the wall downstream of the hump in both A_1 and A_2 cases. Due to successive pressure gradient changes downstream of the hump, the near-wall crossflow velocity component reverses direction within a finite region, $0.156 < x/c_x < 0.177$, located downstream of the hump apex.²⁴ The extent of this region over the wing is marked by the vertical dashed lines in figures 2(a, b) and is bounded by the wall and the white dashed isolines in figures 2(d, f). The FPG over the wing promotes the development of crossflow instabilities (CFIs). As CFIs grow and stationary CF vortices form, they distort the boundary layer (BL), as seen in figures 2(c–f). This distortion is more pronounced in the *high*-amplitude A_2 cases due to the larger amplitude of the stationary vortices.

To investigate the amplification of stationary primary crossflow disturbances within the boundary layer, the steady perturbation velocity field (u'_c, v'_c, w'_c) is extracted from the DNS solution. This is done by subtracting the unperturbed base flow, defined as the spanwise-invariant solution obtained by means of a 2.5D simulation, from the three-dimensional base flow. The spanwise root-mean-square of CF perturbations, i.e., $\langle u'_c \rangle_z$, $\langle v'_c \rangle_z$, and $\langle w'_c \rangle_z$, serves as a measure of their amplitude.³⁰ Figure 3 shows the chordwise evolution of the wall-normal maximum of $\langle u'_c \rangle_z$ for the cases analysed in this study. In the hump A_1 case (red solid line), the chordwise growth rate of stationary CF perturbations decreases compared to the reference A_1 case for $x/c_x > 0.2$. This reduction leads to weaker CF vortices downstream of the hump and results in a significant transition delay in the presence of unsteady disturbances in the BL, as observed in experiments²³ and numerical simulations.²⁴ However, downstream of the hump in *high*-amplitude A_2 case (red dashed line), the amplitude of stationary CF perturbations increases significantly compared to the amplitude of perturbations in the reference A_2 case. This is attributed to the formation of a pair of counter-rotating stationary vortices downstream of the hump in A_2 case.²⁴

INFLUENCE OF SURFACE HUMP ON SECONDARY CROSSFLOW INSTABILITIES

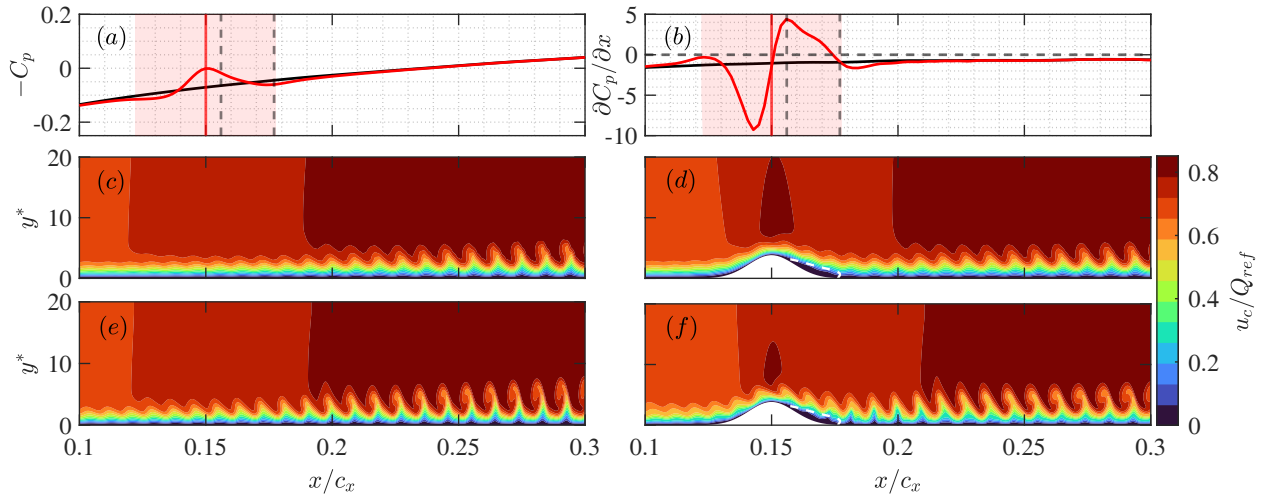


Figure 2: (a) Pressure coefficient, $-C_p = -(p - p_\infty)/(0.5\rho_\infty U_\infty^2)$, and (b) wall pressure gradient $\partial C_p/\partial x$ for reference (black) and hump (red) cases. $\partial C_p/\partial x = 0$ is marked by horizontal black dashed line in panel (b). Contours of chordwise velocity u_c at $z = -\lambda/2$ for (c) reference A_1 , (d) hump A_1 , (e) reference A_2 , and (f) hump A_2 . The CF reversal region is bounded by the wall and the white dashed isolines in panels (d, f). $Q_{\text{ref}} = 23.496$ m/s is the boundary layer edge velocity at the 3D DNS inlet. Contours are shown in the x/c_x - y^* plane, where $y^* = (y_g - y_{g,\text{clean}}^{\text{wall}})/\delta_0$. $\delta_0 = 2.687 \times 10^{-4}$ m is the displacement thickness at inlet of the domain, and $y_{g,\text{clean}}^{\text{wall}}$ is the y_g -coordinate of the wall in the reference clean case. The red solid vertical line marks the hump apex and the shaded region its width.

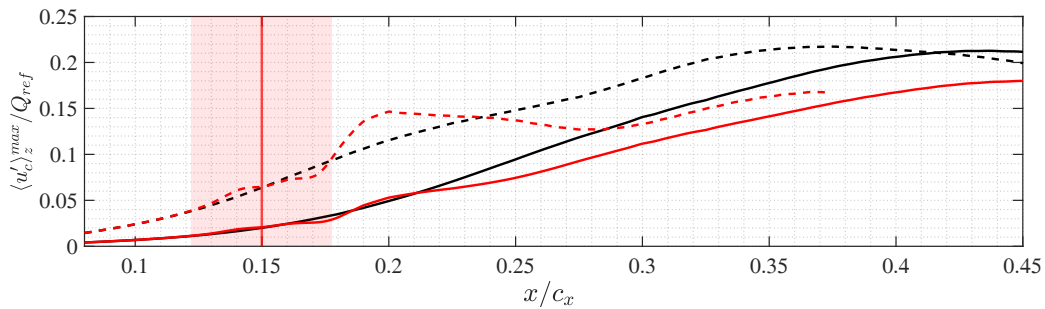


Figure 3: Amplitude of the chordwise component (u_c) of the stationary CF perturbation for the clean (black) and hump (red) cases. Solid lines represent the *low*-amplitude perturbation cases (A_1), while dashed lines represent the *high*-amplitude perturbation cases (A_2). The red solid vertical line marks the hump apex and the shaded region its width.

4. Stability analysis results

This section investigates the secondary crossflow instabilities of the base flows presented in § 3 using LST-2D and PSE-3D approaches.

4.1 Influence of the hump on the standard secondary instabilities

This section investigates how the hump affects the evolution of type I and type II secondary instabilities. These are high-frequency modes driven by spanwise and wall-normal shear, respectively. Ambrosino *et al.*²⁵ demonstrated that a PSE-3D formulation in a curvilinear non-orthogonal coordinate system accurately captures their behaviour over a swept wing, reproducing mode shapes, locations, and growth rates in agreement with DNS data. This methodology is used here to assess the hump's influence, focusing on the type I mode, which is identified as the driving mechanism responsible for triggering the transition in the reference A_1 and A_2 cases.²⁴ LST-2D computations indicate that, for the reference A_1 case, the type I instability exhibits its maximum integrated growth (N -factor) at a frequency of approximately $f \approx 5000$ Hz. Figure 4(a) displays the resolved eigenvalue spectra at $f = 5000$ Hz for both the reference clean and hump A_1 cases, evaluated at the station $x/c_x = 0.4$. It can be noted that the two cases feature different families of unstable high-frequency secondary instabilities. At this frequency, different families of type II instabilities and one

INFLUENCE OF SURFACE HUMPS ON SECONDARY CROSSFLOW INSTABILITIES

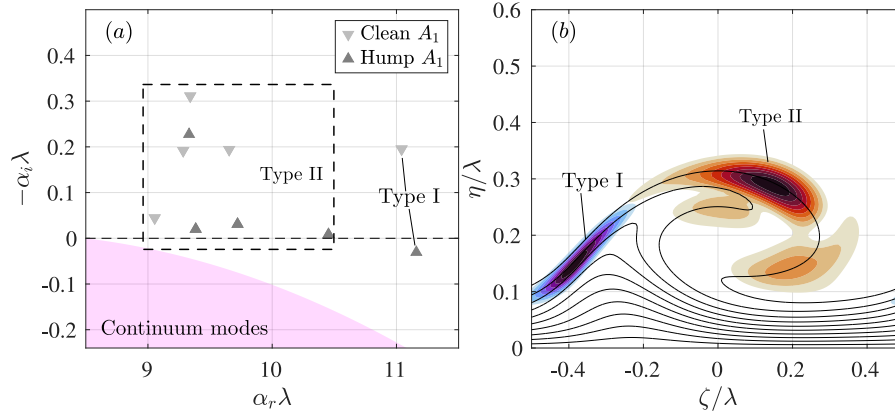


Figure 4: (a) Resolved spatial eigenvalue spectra for the reference (clean) A_1 and hump A_1 cases at the station $x/c_x = 0.4$ at the frequency $f = 5000$ Hz. The eigenvalues enclosed in the dashed rectangle belong to type II modes. Regions with continuous branches of the spectrum are represented by a purple shaded region. (b) Normalized magnitude of the streamwise perturbation velocity component for the type I (blue scale) and most unstable type II (red scale) of the clean A_1 case. The black lines stand for ten equally spaced isolines of the normalized base flow streamwise velocity component, $\bar{u}_c/\bar{u}_{c,\max}$, in the interval $[0, 0.95]$.

type I mode are identified in the spectra. Figure 4(b) shows the normalized magnitude of the streamwise perturbation velocity component for the type I and the most unstable type II modes for reference A_1 case, at the same location and frequency as the spectra in figure 4(a). The corresponding modes for the hump A_1 case are similar in shape and are therefore not shown here. As can be seen, the secondary instabilities shared between the two cases are weaker for the hump A_1 case, and the type I perturbation becomes stable at this location and frequency. In particular, the type I mode is only slightly amplified in the hump A_1 case, with very low growth rates and is unstable only for a short streamwise extent resulting in negligible N -factors. These results are in line with the DNS results for the hump A_1 case.²⁴

The observed weakening of type I instabilities is related to the variation of the spanwise gradient due to the presence of the hump. This originates from the tilting of stationary CF perturbations downstream of the hump and within the CF reversal region (i.e., the region where the CF velocity component changes sign near the wall), which leads to the stabilisation of stationary CF vortices as shown by Rius-Vidales *et al.*²³ and Moniripiri *et al.*²⁴ Figure 5 portrays the maximum and minimum spanwise gradients versus the chordwise coordinate for all the cases. The vertical solid red line indicates the position of the hump and its effect can be seen on the spanwise gradient. The derivatives are normalized as $\partial u/\partial z|_{\min}^* = (\partial u/\partial z)(\delta_0/Q_{ref})$. In particular, immediately downstream of the hump, an increase (in absolute value) of both the maximum and minimum spanwise gradients can be observed. A much stronger amplification is observed in the hump A_2 case. Further downstream, their values are much lower compared with the reference case, indicating a weakening of the stationary crossflow vortex and, as a consequence, of the secondary instabilities. This holds for both the *low*-amplitude A_1 and *high*-amplitude A_2 cases, with a much stronger reduction in the hump A_2 case compared with the reference A_2 case. Note that, since transition to turbulence in the hump A_2 case has been observed at $x/c_x \approx 0.25$ in the experiment²³ and DNS,²⁴ the simulation domain for this case is shorter than other cases to reduce the computational costs. The locations at which the type I mode becomes unstable are displayed by dashed vertical lines. As expected, in the reference A_2 case, the type I mode is amplified much more upstream, with respect to the reference A_1 case, due to a larger amplitude of the crossflow vortex. Interestingly, the values of the normalized spanwise gradients $\partial u/\partial z|_{\min}^*$ at which the type I secondary instability becomes unstable are very close to each other among the different cases (marked by the purple shaded region in figure 5). This indicates that, most likely, there is a threshold above which the mode becomes unstable. Furthermore, for the hump A_2 case, no unstable high-frequency mode was observed within the typical frequency range associated with the type I mode. This suggests that transition in the hump A_2 case is likely driven by other types of secondary instabilities, which may not be present in the reference cases.

4.2 Secondary instabilities induced by the hump

Spatial LST-2D computations were conducted downstream of the hump to determine whether modifications to the base flow caused by the hump give rise to new instability mechanisms. The presence of the hump induces successive APG and FPG regions, which leads to a reversal of the CF velocity component downstream of the hump.²⁴ This leads to

INFLUENCE OF SURFACE HUMP ON SECONDARY CROSSFLOW INSTABILITIES

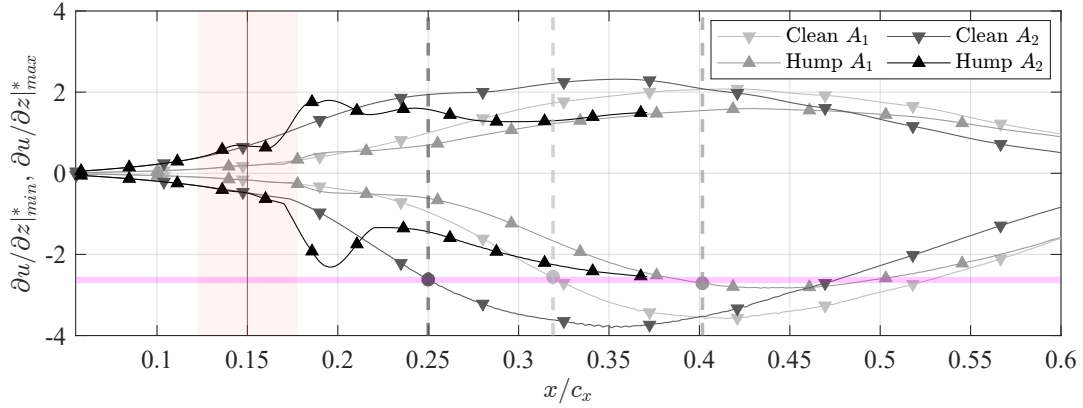


Figure 5: Maximum and minimum spanwise gradient versus the chordwise direction for the reference (clean) and hump cases for both *low-* and *high-*amplitude cases. The red solid vertical line marks the hump apex and the shaded region its width. The dashed vertical lines indicate the location of the neutral point for the type I secondary instabilities, color-coded accordingly to the case. The purple shaded area represents the range of $\partial u / \partial z$ at the first location where the type I is amplified.

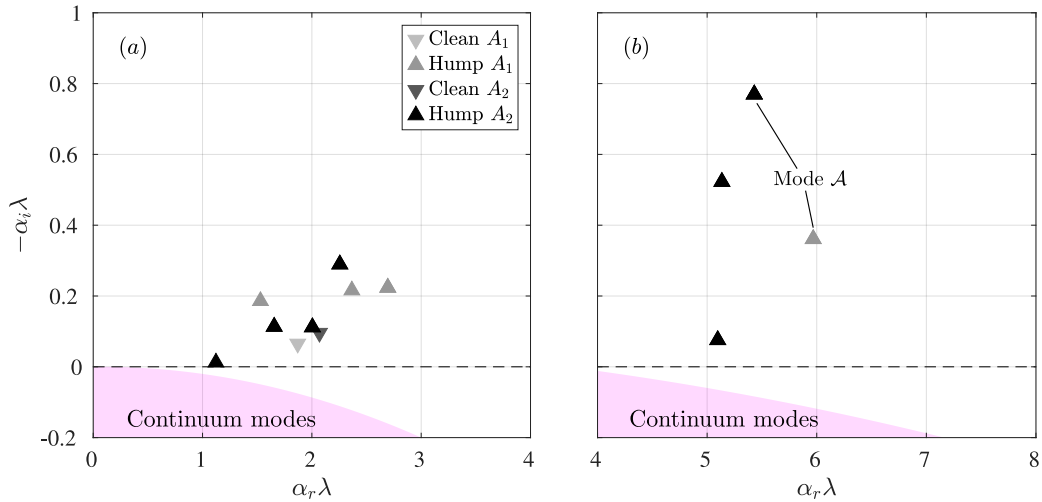


Figure 6: Resolved spatial eigenvalue spectra for the reference clean and hump A_1 and A_2 cases. The eigenvalue spectra are computed at the station $x/c_x = 0.176$ at (a) $f = 500$ Hz and (b) $f = 1200$ Hz. Regions with continuous branches of the spectra are represented by a purple solid shaded region.

the appearance of additional inflection points in the CF velocity component profile. Consequently, the flow becomes susceptible to several additional instabilities that do not occur in the reference cases. Figure 6 provides the spatial eigenvalue spectra for the reference and hump cases at the *low-* and *high-*amplitude of the crossflow instability. The spectra are computed at the chordwise location of $x/c_x = 0.176$ for the frequencies $f = 500$ Hz (figure 6(a)) and $f = 1200$ Hz (figure 6(b)). The hump cases are characterised by several families of unstable modes and several continuous branches, which lie in the stable portion of the spectra and represent modes living in the free stream. The reference cases only feature one mode at the lower frequency ($f = 500$ Hz), whereas they do not display any unstable mode at the larger frequency ($f = 1200$ Hz). The unstable mode at $f = 500$ Hz in the reference (clean) cases corresponds to the primary travelling crossflow instability, modulated by the interaction with the stationary crossflow vortex. As expected, the growth rate of the mode in the reference A_2 case is larger because of the larger amplitude of the stationary crossflow vortex (cf. figure 3). The normalized magnitude of the streamwise velocity component amplitude functions of these modes, based on a LST-2D computation, for the reference and hump A_1 and A_2 cases are shown in figure 7. As one can see, in the reference *low-*amplitude case, the crossflow vortex is less strong and the mode is just a mild modulation of a travelling crossflow instability. In the *high-*amplitude A_2 case, the stationary crossflow vortex is more developed and a clear type III secondary instability is recognizable in the region close to the wall. Notably, in the hump cases at $f = 500$ Hz, there are several additional instabilities which are excited. An inspection of the amplitude shape

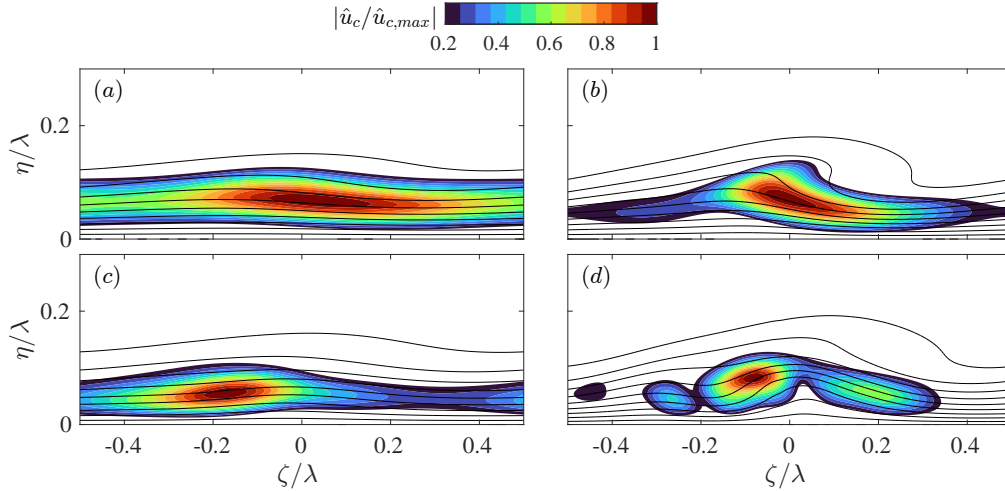


Figure 7: Normalized magnitude of the streamwise perturbation velocity component at the frequency $f = 500$ Hz and at the station $x/c = 0.176$ for (a) reference A_1 , (b) reference A_2 , (c) hump A_1 , and (d) hump A_2 . The modes in the hump cases correspond to the second most unstable modes in figure 6(a). The black lines stand for ten equally spaced isolines of the normalized base flow streamwise velocity component \bar{u}/\bar{u}_{max} , in the interval $[0, 0.95]$.

of those instabilities reveals that all these modes have similar spatial distributions and resemble a modulated travelling crossflow instability/type III whose shape is affected by the presence of the hump. The eigenfunctions corresponding to the second most unstable eigenvalues in figure 6(a) for hump A_1 and A_2 cases are shown in figures 7(c, d).

To relate the velocity perturbation of the amplified modes to the distortion of the flow field, the base flow velocity gradients at the station $x/c_x = 0.176$ are shown in figure 8 for the cases under study. In particular, the wall-normal shear is portrayed in figures 8(a, c, e, g), while the spanwise gradients are shown in figures 8(b, d, f, h). Note that the gradients have been normalized with the maximum values of the hump A_2 case for a direct comparison. As can be seen, the velocity gradients of the hump A_1 case are just a mild modification of the ones in the reference A_1 case. In particular, the region where the spanwise shear attains its maximum value is slightly deformed (cf. figure 8(f)). On the other hand, the effect of the hump in the *high-amplitude* A_2 case is more pronounced and strongly impacts the instability characteristics of the boundary layer downstream of the hump. In particular, on the upwash and downwash sides of the crossflow vortex, there is an area of increased wall-normal shear, and the spanwise shear displays a strong distortion. The area of negative spanwise velocity gradient is split into two, and a region of positive values appears in between, indicating the presence of an additional vortex. This additional vortex is visible in figure 9(b) and is referred to as hump-induced vortex (hump-IV).

Figure 9 portrays the leading instabilities for the frequency $f = 1200$ Hz at $x/c_x = 0.176$ (cf. figure 6(b)), denoted as mode \mathcal{A} , for the hump A_1 and hump A_2 cases. Note that this mode is only unstable in the hump cases. As shown in the figure, the dominant modes in the two hump cases feature a region of large amplitude in the region under the crossflow vortex, close to the wall. The presence of the additional hump-induced vortex strongly influences the structure of the dominant mode \mathcal{A} at this station and more downstream (see § 4.3). The mode \mathcal{A} in the hump A_2 case features a region of large amplitude and an additional zone with local maxima on its side on top of the hump-IV. On the other hand, the largest amplitude is mainly concentrated in the region between the CF vortex (CFV) and the hump-IV. According to figures 8(g, h), these locations are associated with large wall-normal and spanwise gradients, induced by the hump, which deforms the CFV and promotes additional shear stresses.

4.3 Streamwise evolution of mode \mathcal{A}

In this section, the streamwise evolution of the growth rates and N -factors of the mode \mathcal{A} in the hump A_2 case are investigated to clarify the role of this perturbation and its impact on the instability properties of the boundary layer downstream of the hump. Figure 10(a) displays the evolution of the dimensional spatial growth rate of the mode \mathcal{A} computed via LST-2D for four different frequencies. The curves associated with modes with different frequencies exhibit similar behaviour. Mode amplification begins slightly downstream of the hump apex, coinciding with the reversal of the CF velocity component near the wall. The mode then undergoes rapid amplification, reaching growth rates on the order of 250 1/m, followed by a sudden drop, a "plateau" region, and eventual stabilization. It is observed that with increasing frequency, the peak growth rate becomes higher, followed by a more rapid decay. Lower-frequency modes are

INFLUENCE OF SURFACE HUMP ON SECONDARY CROSSFLOW INSTABILITIES

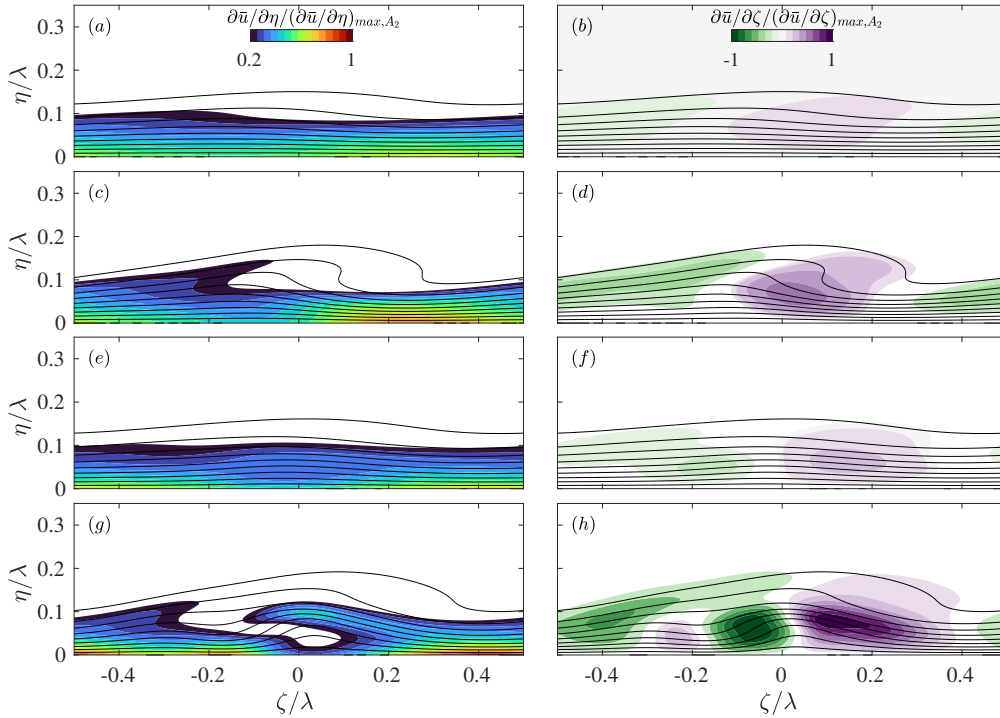


Figure 8: Base flow gradients at the station $x/c_x = 0.176$ for the (a, b, c, d) reference and (e, f, g, h) hump cases. Low-amplitude A_1 cases represented in (a, b, e, f) and high-amplitude A_2 cases in (c, d, g, h). Normalized gradients of the base flow streamwise velocity component with respect to the wall-normal direction (a, c, e, g) and the spanwise direction (b, d, f, h). Contour levels below $\partial\bar{u}/\partial\eta/(\partial\bar{u}/\partial\eta)_{max, A_2} < 0.2$ are blanked out in (a, c, e, g) and normalized gradients between 15% of the maximum and minimum shear are blanked out in (b, d, f, h). The black lines stand for ten equally spaced isolines of the normalized base flow streamwise velocity component \bar{u}/\bar{u}_{max} , in the interval $[0, 0.95]$.

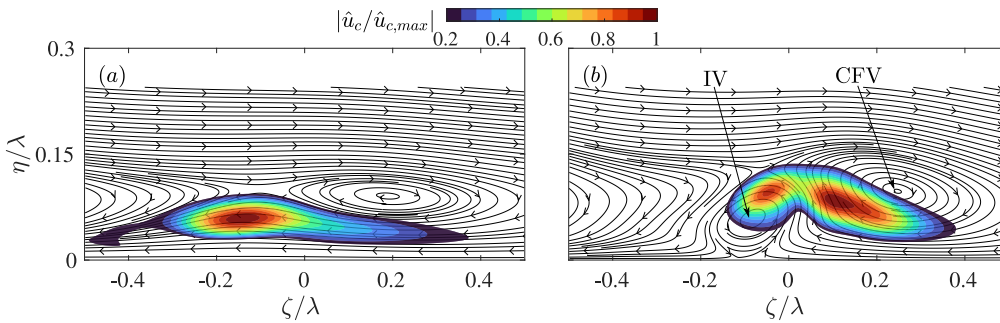


Figure 9: Normalized magnitude of the streamwise velocity component amplitude function of the leading instabilities at the frequency $f = 1200$ Hz and at the station $x/c_x = 0.176$ for the (a) hump A_1 and (b) hump A_2 cases. The black solid lines represent the cross-sectional streamlines represented by the in-plane velocity components $(v - w)$. CFV and IV stand for crossflow and hump-induced vortex, respectively.

associated with smaller peak growth rates; however, the mode remains unstable over a longer chordwise extent, resulting in larger integrated growth. This is illustrated in figure 10(b), which shows the N -factor envelope (black thick line). As one can see, the N -factor envelope exhibits two local maxima: the first occurs around $x/c_x \approx 0.19$, corresponding to the modes with higher-frequencies, while the second, more pronounced maximum appears near $x/c_x \approx 0.21$, associated with the lower-frequency curves of mode \mathcal{A} . The N -factor envelope for mode \mathcal{A} in the hump A_1 case is represented by the thick grey line in figure 10(b). In this configuration, the mode exhibits only weak growth starting at the onset of the CF reversal region and decays rapidly downstream. Notably, the counter-rotating vortex pair observed in the hump A_2 case does not develop downstream of the hump in the A_1 configuration. Figure 11 provides the streamwise evolution of the shape of the mode \mathcal{A} at several stations downstream of the hump (A_2 case). At the first station, a hump-induced vortex emerges near the wall, exerting a strong influence on the developing perturbation. As shown in figure 11(b),

INFLUENCE OF SURFACE HUMP ON SECONDARY CROSSFLOW INSTABILITIES

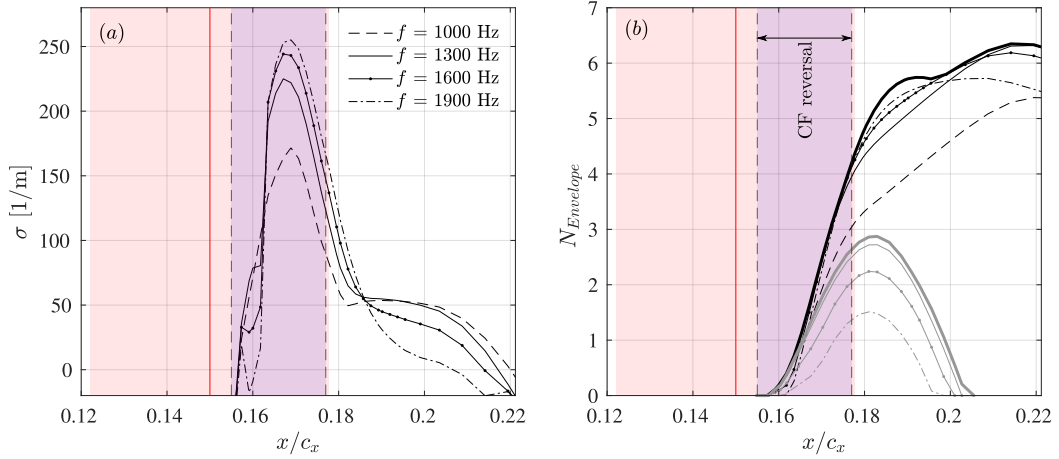


Figure 10: (a) Streamwise evolution of σ at four different frequencies of the mode \mathcal{A} and (b) the corresponding N -factors and envelope (black thick line) downstream of the hump A_2 . The grey lines in (b) indicate the N -factor curves and envelope for the mode \mathcal{A} in the hump A_1 . The solid vertical red line marks the hump apex and the shaded region its width. The shaded regions enclosed by the vertical dashed lines indicate the extent of the CF reversal region.

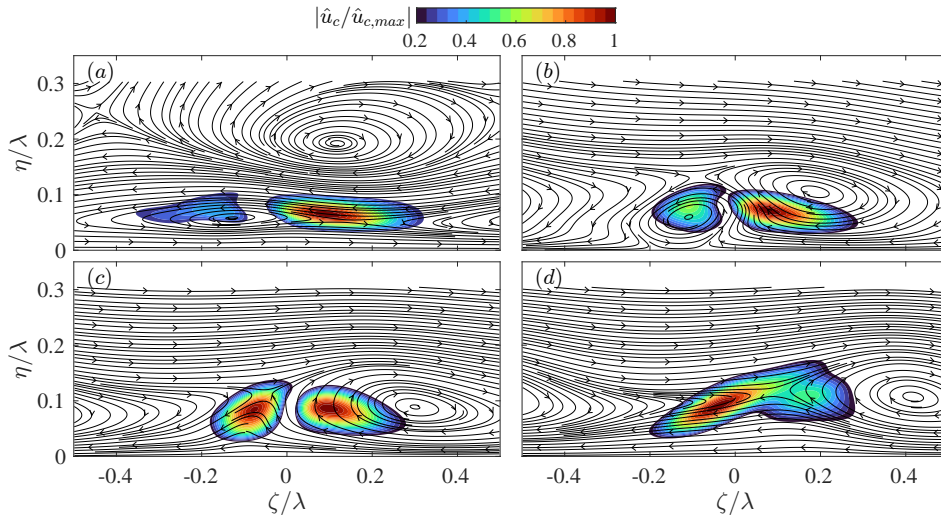


Figure 11: Mode \mathcal{A} downstream of the hump (A_2 case) at the stations (a) $x/c_x = 0.167$, (b) $x/c_x = 0.182$, (c) $x/c_x = 0.1919$ and (d) $x/c_x = 0.207$, at the frequency $f = 1200$ Hz. The black lines represent the vortex system by the in-plane velocity components ($v - w$).

the mode is 'split' with two distinct regions of large amplitude. Moving downstream, the perturbation on the left side becomes stronger than the one on the right side. As the hump-IV vanishes, these two local amplitude maxima merge into a single structure localised on the upwash side of the crossflow vortex, resembling a type I secondary instability. However, the frequency of this mode ($f = 1200$ Hz) is lower than the typical frequency associated with the type I mode ($f = 5000$ Hz) in the reference A_1 and A_2 cases. Finally, figure 12 portrays a three-dimensional view of the mode \mathcal{A} at the frequency $f = 1200$ Hz in the non-orthogonal coordinate system, based on a PSE-3D computation. Alternating strips of positive and negative values of the real part of the streamwise velocity component aligned with the direction of the crossflow vortex are observed close to the hump location. Further downstream of the hump, these strips become increasingly inclined, reflecting the rotation direction of the crossflow vortex.

5. Comparison between instability analysis and DNS

This section compares DNS and instability results for unsteady perturbations downstream of the hump A_2 . The perturbation is extracted from the DNS by decomposing the velocity field through a Fourier transformation in time and isolating the frequency of interest. PSE-3D results are transformed back into the orthogonal curvilinear coordinate

INFLUENCE OF SURFACE HUMPS ON SECONDARY CROSSFLOW INSTABILITIES

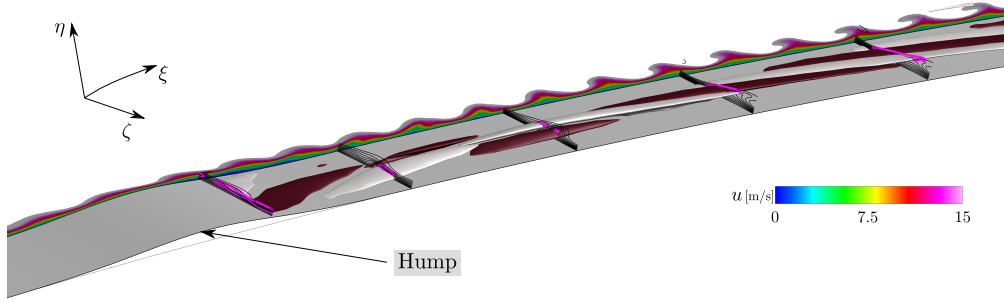


Figure 12: Mode \mathcal{A} at $f = 1200$ Hz downstream of the hump A_2 represented by red (positive) and white (negative) three-dimensional isosurfaces of the normalized real part of the streamwise velocity component amplitude function ($\hat{u}_r/\hat{u}_{r,max} = \pm 0.01$) in the range $x/c_x \in [0.155, 0.24]$. Isolines of the streamwise velocity component of the distorted base flow in solid black and normalized magnitude of the streamwise velocity amplitude function represented by a purple isoline ($|\hat{u}/\hat{u}_{max}| = 0.5$).

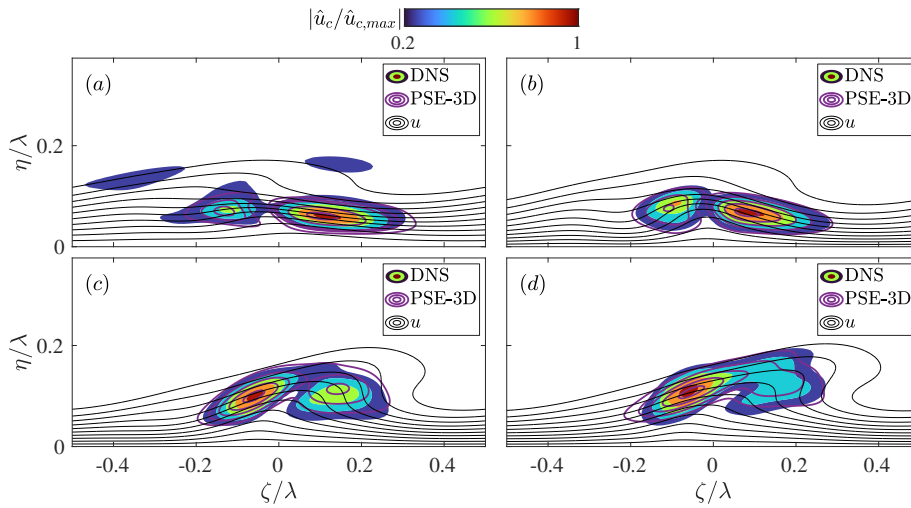


Figure 13: Normalized magnitude of the streamwise velocity component amplitude function ($|\hat{u}_c/\hat{u}_{c,max}|$) for the mode \mathcal{A} of figure 6 at the frequency $f = 1200$ Hz, shown at the stations (a) $x/c_x = 0.172$, (b) $x/c_x = 0.184$, (c) $x/c_x = 0.202$ and (d) $x/c_x = 0.22$. DNS (filled contour) compared with PSE-3D (purple isolines). The black lines stand for ten equally spaced isolines of the normalized base flow streamwise velocity component, $\bar{u}_c/\bar{u}_{c,max}$, in the interval $[0, 0.95]$.

system for a direct comparison. The frequency $f = 1200$ Hz is considered for the comparison. Both the DNS and the instability computations feature a dominant perturbation that is located close to the wall, on the upper side of the additional hump-IV. Figure 13 portrays a comparison between the DNS and PSE-3D results, for $|\hat{u}_c/\hat{u}_{c,max}|$. Several stations downstream of the hump and upstream of the transition region are considered. It can be noted that PSE-3D computations can recover the main features of the unsteady perturbation, accurately reflecting the location and shape of the mode, with a strong overall correlation observed with the DNS results at all the stations. Figure 14 compares the integrated growth rate (i.e., the N -factor) obtained from instability computations with the one extracted from the DNS. The N -factors data (DNS, LST-2D, and PSE-3D) are based on the integral of the disturbance kinetic energy across the plane $\eta\zeta$. The DNS-based N -factor curve is normalized at $x/c_x \approx 0.17$, which is the first station where a perturbation resembling mode \mathcal{A} can be clearly isolated. Upstream of this location, the perturbations extracted from the DNS do not consist of only a pure hump-induced secondary instability. Instead, they include contributions from other perturbations at the same frequency. This is a consequence of the random forcing employed in the DNS. This is clarified by the insets in figure 14, which depict the Fourier-transformed perturbation from the DNS at the frequency $f = 1200$ Hz at two different chordwise locations. The stations upstream of $x/c_x \approx 0.17$ feature a large perturbation on top of the stationary CFV. Performing the integral of the kinetic energy in the plane $\eta\zeta$ to obtain the N -factor at these locations results in overestimating values which are not comparable with the results from the instability computation. Indeed, both LST-2D and PSE-3D solve exclusively for a single, well-defined mode, i.e. mode \mathcal{A} . It is here underlined that this may also contribute to the small differences noted between the PSE-3D and DNS results on the amplitude functions

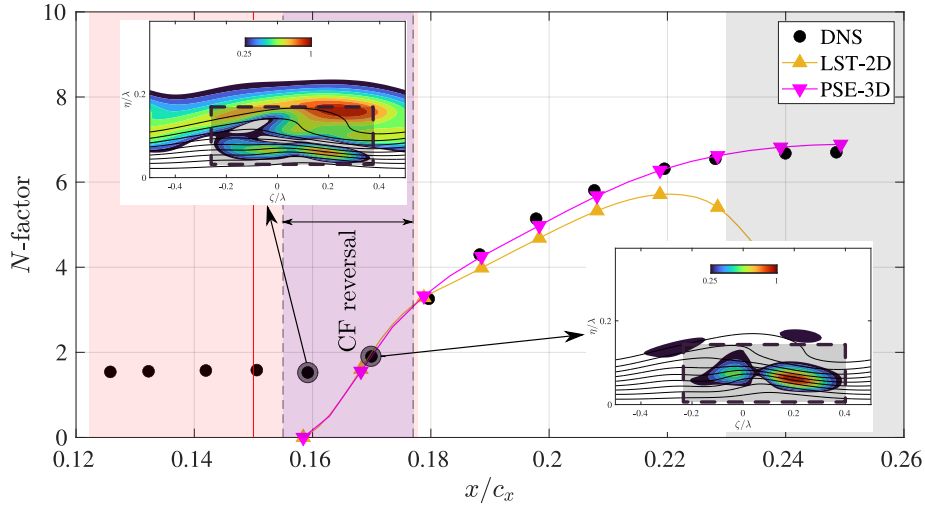


Figure 14: N -factor curves versus x/c_x for the mode \mathcal{A} in figure 6 for the frequency $f = 1200$ Hz in the hump A_2 case: DNS, LST-2D, and PSE-3D. The insets display a zoom of the perturbation distribution (chordwise velocity component) computed from the DNS at two different chordwise locations. The rectangular grey-shaded area in the insets of the figure indicates the spatial region where the mode is amplified. The red solid vertical line marks the hump apex and the shaded region its width. The shaded region enclosed in the dashed lines indicates the area of CF reversal. The grey-shaded area portrays the region where the flow becomes transitional in the DNS.

shown in figure 13. LST-2D results underestimate the N -factor compared to normalized DNS results, consistent with the observation of Ambrosino *et al.*²⁵ In contrast, the PSE-3D computation yields larger growth rates compared to the LST-2D ones and closely matches the amplification observed in the DNS. The significant deviation between the LST-2D and PSE-3D curves confirms that the streamwise gradients of the base flow and of the amplitude function play a non-negligible role in predicting the amplification of the disturbance. Both the normalized DNS and linear stability results exhibit an N -factor of approximately 7 in the region where the DNS indicates transition, suggesting strong perturbation growth. This large amplification, associated with mode \mathcal{A} , implies that a strong convective instability could be responsible for the transition in the hump A_2 case, consistent with the findings of Moniripiri *et al.*²⁴ While the reference A_2 case undergoes transition due to the growth of the type I secondary instability of the stationary CFV,²⁴ the presence of the hump alters the transition scenario. Specifically, when sufficiently strong crossflow vortices interact with the hump, the transition front moves upstream. This shift is attributed to the hump-induced secondary instability developing downstream of the hump. The strong agreement between linear instability predictions and DNS, both in mode structure and N -factor distribution, reinforces the conclusion that the transition mechanism remains governed by modal perturbation growth.

6. Conclusions

This study investigates the evolution of unsteady disturbances downstream of a smooth surface hump in a crossflow-dominated boundary layer over a swept wing by means of instability analysis. The objective is to assess the applicability of linear stability theory in analysing such configurations. This is examined through a quantitative comparison between instability predictions and DNS results. The two-dimensional local theory (LST-2D) and linear three-dimensional plane-marching parabolized stability equation (PSE-3D) methodologies are employed to study the effect of a smooth surface hump geometry on the swept-wing boundary layer corresponding to the experiments by Rius-Vidales *et al.*²³ They experimentally investigated the interactions between a smooth surface hump and steady crossflow perturbations with *low*- and *high*-amplitudes.

Stability analyses are conducted to examine the evolution of secondary instabilities of stationary crossflow vortices and to identify how these are affected by the hump. Spatial LST-2D have been performed downstream of the surface hump to identify the most relevant modes and most unstable disturbance frequencies. The spatial eigenvalue spectra reveal the existence of several instabilities amplified in the downstream of the hump for both *low*- and *high*-amplitude cases. In both cases, a dominant mode, denoted as mode \mathcal{A} , is identified. In the hump A_1 case the mode \mathcal{A} is amplified in a short streamwise extent and does not reach large N -factor values. Therefore, it is concluded that this mode does not affect the transition mechanism. As a consequence, by performing PSE-3D computations, the be-

INFLUENCE OF SURFACE HUMP ON SECONDARY CROSSFLOW INSTABILITIES

haviour of the type I perturbations was analysed to identify the frequencies which lead to the largest amplification of the disturbance. Moreover, in the experiment²³ and DNS,²⁴ the hump A_1 case exhibits a delayed transition compared to the clean case. This is confirmed here by the instability computations, which show a weakening of the type I secondary instability mechanism. In particular, the stability analysis for hump A_1 case reveals an amplified type I only for a very small streamwise extent and very low growth rates, which results in negligible N -factors. These results are consistent with a downstream movement of the transition front, as observed in experiments²³ and DNS.²⁴

On the other hand, the hump A_2 case displays a different transition mechanism in the DNS and experiment, with the transition front moving upstream near the smooth hump. Finally, a comparison between the instability computations and DNS data demonstrates that the PSE-3D simulations accurately capture the mode's location and perturbation shape, showing overall good agreement at various downstream positions relative to the hump. Furthermore, an analysis of the N -factor curve for a frequency of $f = 1200$ Hz reveals that LST-2D significantly underestimates mode amplification, whereas the PSE-3D results closely align with the amplification trends observed in the DNS. Moreover, both the PSE-3D and normalized DNS results exhibit a maximum N -factor of approximately $N \approx 7$ in the region where the DNS indicates the onset of transition. The significant amplification of mode \mathcal{A} by a factor of $e^7 \approx 1100$ aligns with the observed transition in the DNS. This finding reinforces the idea that this perturbation is the primary driver of the early laminar-to-turbulent transition process in the hump A_2 case.²⁴ Lastly, the strong quantitative agreement between linear stability theory and DNS suggests that the transition scenario in the hump A_2 case is governed by a modal growth of perturbations.

Acknowledgments

B.A. and M.M. have received funding from the European Union's Horizon 2020 research and innovation programme under the Marie Skłodowska-Curie grant agreement No. 955923. M.K. has received funding from the Dutch Research Council (NWO), under the Vici programme (grant agreement 20647). The computations were enabled by resources provided by the National Academic Infrastructure for Supercomputing in Sweden (NAISS), partially funded by the Swedish Research Council through grant agreement no. 2022-06725.

References

- [1] A. Washburn, R. Campbell, W. Saric, I. Wygnanski, E. Baumann, and R. King, "Drag reduction status and planar laminar flow and AFC," in *AIAA Aero Sciences Meeting*, American Institute of Aeronautics and Astronautics, 2011.
- [2] A. F. Rius-Vidales and M. Kotsonis, "Impact of a forward-facing step on the development of crossflow instability," *Journal of Fluid Mechanics*, vol. 924, p. A34, 2021.
- [3] A. F. Rius-Vidales and M. Kotsonis, "Unsteady interaction of crossflow instability with a forward-facing step," *Journal of Fluid Mechanics*, vol. 939, p. A19, 2022.
- [4] P. S. Klebanoff and K. D. Tidstrom, "Mechanism by which a two-dimensional roughness element induces boundary-layer transition," *Physics of Fluids (PFL)*, vol. 15, no. 7, pp. 1173–1188, 1972.
- [5] M. Moniripiri, P. P. C. Brito, A. V. G. Cavalieri, N. R. Sêcco, and A. Hanifi, "An adjoint-based methodology for calculating manufacturing tolerances for natural laminar flow airfoils susceptible to smooth surface waviness," *Theoretical and Computational Fluid Dynamics*, vol. 38, no. 1, pp. 15–37, 2024.
- [6] W. Saric, H. Reed, and E. White, "Stability and transition of three-dimensional boundary layers," *Annual Review of Fluid Mechanics*, vol. 35, no. 1, pp. 413–440, 2003.
- [7] L. M. Mack, "Boundary layer linear stability theory," *Special Course on Stability and Transition of Laminar Flow, AGARD 709*, 1984.
- [8] H. Bippes, "Basic experiments on transition in three-dimensional boundary layers dominated by crossflow instability," *Progress in Aerospace Sciences*, vol. 35, no. 4, pp. 363–412, 1999.
- [9] L.-U. Schrader, L. Brandt, and D. S. Henningson, "Receptivity mechanisms in three-dimensional boundary-layer flows," *Journal of Fluid Mechanics*, vol. 618, pp. 209–241, 2009.
- [10] W. Koch, F. P. Bertolotti, A. Stolte, and S. Hein, "Nonlinear equilibrium solutions in a three-dimensional boundary layer and their secondary instability," *Journal of Fluid Mechanics*, vol. 406, pp. 131–174, 2000.

INFLUENCE OF SURFACE HUMP ON SECONDARY CROSSFLOW INSTABILITIES

- [11] M. R. Malik, F. Li, M. M. Choudhari, and C.-L. Chang, “Secondary instability of crossflow vortices and swept-wing boundary-layer transition,” *Journal of Fluid Mechanics*, vol. 399, pp. 85–115, 1999.
- [12] J. Serpieri and M. Kotsonis, “Three-dimensional organisation of primary and secondary crossflow instability,” *Journal of Fluid Mechanics*, vol. 799, pp. 200–245, 2016.
- [13] M. Högberg and D. Henningson, “Secondary instability of cross-flow vortices in Falkner-Skan-Cooke boundary layers,” *Journal of Fluid Mechanics*, vol. 368, pp. 339–357, 1998.
- [14] E. B. White and W. S. Saric, “Secondary instability of crossflow vortices,” *Journal of Fluid Mechanics*, vol. 525, pp. 275–308, 2005.
- [15] F. Li and M. M. Choudhari, “Spatially developing secondary instabilities in compressible swept airfoil boundary layers,” *Theoretical and Computational Fluid Dynamics*, vol. 25, pp. 65–84, 2011.
- [16] K. J. Groot, E. S. Beyak, D. T. Heston, and H. L. Reed, “Boundary-layer stability of a natural-laminar-flow airfoil,” in *AIAA Scitech 2020 Forum*, 2020.
- [17] J. L. Eppink, “Mechanisms of stationary cross-flow instability growth and breakdown induced by forward-facing steps,” *Journal of Fluid Mechanics*, vol. 897, p. A15, 2020.
- [18] A. F. Rius-Vidales and M. Kotsonis, “Influence of a forward-facing step surface irregularity on swept wing transition,” *AIAA Journal*, vol. 58, pp. 5243–5253, Dec 2020.
- [19] M. W. Tufts, H. L. Reed, B. K. Crawford, J. G. T. Duncan, and W. S. Saric, “Computational investigation of step excrescence sensitivity in a swept-wing boundary layer,” *Journal of Aircraft*, vol. 54, no. 2, pp. 602–626, 2017.
- [20] K. J. Groot and J. L. Eppink, “Stability analysis of the flow over a swept forward-facing step using PIV base flows,” *American Institute of Aeronautics and Astronautics*, 2021-0966, January 2021.
- [21] F. Tocci, G. Chauvat, A. F. Rius-Vidales, M. Kotsonis, A. Hanifi, and S. Hein, “Interaction of crossflow modes with forward-facing steps: insights gained from DNS,” in *IUTAM Laminar-Turbulent Transition: 10th IUTAM Symposium*, 2024.
- [22] A. F. Rius-Vidales and M. Kotsonis, “Impact of a forward-facing step on the development of crossflow instability,” *Journal of Fluid Mechanics*, vol. 924, no. A34, pp. 1–14, 2021.
- [23] A. F. Rius-Vidales, L. Morais, S. Westerbeek, J. Casacuberta, M. Soyler, and M. Kotsonis, “Delay of swept-wing transition using a surface hump,” *Journal of Fluid Mechanics*, vol. 1014, p. A35, 2025.
- [24] M. Moniripiri, A. F. Rius-Vidales, M. Kotsonis, , and A. Hanifi, “Direct numerical simulation of the effects of a smooth surface hump on transition in swept-wing boundary layers,” *Journal of Fluid Mechanics (To be submitted)*, 2025.
- [25] B. Ambrosino, F. Tocci, A. Theiß, S. Hein, and D. Rodríguez, “Stationary crossflow vortices’ secondary instability: Linear stability theory and parabolized stability equations,” *AIAA Journal*, pp. 1–17, 2025.
- [26] P. Fischer, J. Lottes, and S. Kerkemeier, “Nek5000 web page,” 2008.
- [27] F. Bertolotti, T. Herbert, and P. Spalart, “Linear and nonlinear stability of the blasius boundary layer,” *Journal of Fluid Mechanics*, vol. 242, pp. 441–474, 1992.
- [28] S. M. Hosseini, R. Vinuesa, P. Schlatter, A. Hanifi, and D. S. Henningson, “Direct numerical simulation of the flow around a wing section at moderate Reynolds number,” *International Journal of Heat and Fluid Flow*, vol. 61, pp. 117–128, oct 2016.
- [29] M. Hermanns and J. A. Hernández, “Stable high-order finite-difference methods based on non-uniform grid point distributions,” *International Journal for Numerical Methods in Fluids*, vol. 56, no. 3, pp. 233–255, 2008.
- [30] R. S. Downs and E. B. White, “Free-stream turbulence and the development of cross-flow disturbances,” *Journal of Fluid Mechanics*, vol. 735, pp. 347–380, 2013.